

KINEMATICS AND CHEMISTRY OF RECENTLY DISCOVERED RETICULUM 2 AND HOROLOGIUM 1 DWARF GALAXIES

SERGEY E. KOPOSOV,¹ ANDREW R. CASEY,¹ VASILY BELOKUROV,¹ JAMES R. LEWIS,¹ GERARD GILMORE,¹ CLARE WORLEY,¹ ANNA HOURIHANE,¹ T. BENSBY,² A. BRAGAGLIA,³ M. BERGEMANN,⁴ G. CARRARO,⁵ E. FLACCOMIO,⁶ U. HEITER,⁷ V. HILL,⁸ P. JOFRE,¹ P. DE LAVERNY,⁸ L. MONACO,⁹ L. SBORDONE,^{10,11} Š. MIKOLAITIS,¹² AND N. RYDE²

¹ Institute of Astronomy, Madingley Road, Cambridge CB3 0HA, UK

² Lund Observatory, Department of Astronomy and Theoretical Physics, Box 43, SE-221 00 Lund, Sweden

³ INAF - Osservatorio Astronomico di Bologna, via Ranzani 1, 40127, Bologna, Italy

⁴ Max-Planck Institut für Astronomie, Königstuhl 17, 69117 Heidelberg, Germany

⁵ European Southern Observatory, Alonso de Cordova 3107 Vitacura, Santiago de Chile, Chile

⁶ INAF - Osservatorio Astronomico di Palermo, Piazza del Parlamento 1, 90134, Palermo, Italy

⁷ Department of Physics and Astronomy, Uppsala University, Box 516, SE-751 20 Uppsala, Sweden

⁸ Laboratoire Lagrange (UMR7293), Université de Nice Sophia Antipolis,

CNRS, Observatoire de la Côte d'Azur, CS 34229, F-06304 Nice cedex 4, France

⁹ Departamento de Ciencias Físicas, Universidad Andrés Bello, República 220, 837-0134 Santiago, Chile

¹⁰ Millennium Institute of Astrophysics, Av. Vicuña Mackenna 4860, 782-0436 Macul, Santiago, Chile

¹¹ Pontificia Universidad Católica de Chile, Av. Vicuña Mackenna 4860, 782-0436 Macul, Santiago, Chile

¹² Institute of Theoretical Physics and Astronomy, Vilnius University, A. Goštauto 12, LT-01108 Vilnius

Received 2015 April XX; accepted 2015 YYYYYYY XX; published 2015 YYYYYYY XX

ABSTRACT

Photometry alone is not sufficient to unambiguously distinguish between ultra-faint star clusters and dwarf galaxies because of their overlap in morphological properties. Accurate measurements of the intrinsic velocity and metallicity dispersions are required to robustly classify such objects. Here we report on VLT/GIRAFFE spectra of candidate member stars in two recently discovered ultra-faint satellites Reticulum 2 and Horologium 1, obtained as part of the ongoing Gaia-ESO Survey. We identify 18 members in Reticulum 2 and 5 in Horologium 1. We find Reticulum 2 to have a velocity dispersion of $3.22^{+1.64}_{-0.49}$ km s⁻¹, implying a M/L ratio of ~ 500 . We have inferred stellar parameters (T_{eff} , $\log g$, $[\text{Fe}/\text{H}]$, $[\alpha/\text{Fe}]$) for all candidates and we find Reticulum 2 to have a mean metallicity of $[\text{Fe}/\text{H}] = -2.46^{+0.09}_{-0.10}$, with an intrinsic dispersion of $0.29^{+0.13}_{-0.05}$ dex, and is α -enhanced to the level of $[\alpha/\text{Fe}] \sim 0.4$ dex. We conclude that Reticulum 2 is a dwarf galaxy. We also report on the serendipitous discovery of four stars in a previously unknown stellar substructure near Reticulum 2 with $[\text{Fe}/\text{H}] \sim -2$ and $V_{\text{hel}} \sim 220$ km s⁻¹, far from the systemic velocity of Reticulum 2 at $V_{\text{hel}} = 64.7^{+1.3}_{-0.8}$ km s⁻¹. For Horologium 1 we infer a velocity dispersion of $\sigma(V) = 4.9^{+2.8}_{-0.9}$ km s⁻¹ and a consequent M/L ratio of ~ 600 , leading us to conclude that Horologium 1 is also a dwarf galaxy. Horologium 1 is slightly more metal-poor than Reticulum 2 ($[\text{Fe}/\text{H}] = -2.76^{+0.1}_{-0.1}$) and is similarly α -enhanced: $[\alpha/\text{Fe}] \sim 0.3$ dex. Despite a large error-bar, we also measure a significant spread of metallicities ($\sigma([\text{Fe}/\text{H}]) = 0.17^{+0.20}_{-0.03}$ dex) which strengthen the evidence that Horologium 1 is indeed a dwarf galaxy. The line-of-sight velocity of Reticulum 2 is offset by some 100 km s⁻¹ from the prediction of the orbital velocity of the LMC, thus making its association with the Cloud uncertain. However, at the location of Horologium 1, both the backward integrated LMC's orbit and the LMC's halo are predicted to have radial velocities similar to that of the dwarf. Therefore, it is very likely that Horologium 1 is or once was a member of the Magellanic Family.

Subject headings: Galaxy: halo, galaxies: dwarf, globular clusters: general, galaxies: kinematics and dynamics, stars: abundances, galaxies: abundances

1. INTRODUCTION

The total inventory of satellites associated with the Milky Way remains incomplete. This is particularly true for the faintest systems, as observations are inherently biased towards finding and characterising intrinsically bright satellites. As a consequence, any inferences on the total satellite luminosity or mass distributions strongly depend on systematic and selection effects in the least luminous systems. Deep, uniform photometry is required to find these relics, and spectroscopy is required for proper characterisation.

Wide-field photometric surveys can be extremely successful at finding Galactic satellites (Willman et al. 2005a,b; Zucker et al. 2006a,b; Belokurov et al. 2006, 2007, 2008, 2009, 2010; Irwin et al. 2007; Koposov et

al. 2007; Walsh et al. 2007; Grillmair 2009; Balbinot et al. 2013). The Sloan Digital Sky Survey (SDSS, Abazajian et al. 2009; Alam et al. 2015) data unveiled more than a dozen systems, opening entire new sub-fields of astrophysics devoted to understanding these satellites and their trailing debris (see reviews by Willman 2010 and Belokurov 2013; see also Casey et al. 2012, 2013, 2014; Martin et al. 2013; Koposov et al. 2013; Deason et al. 2014; de Boer et al. 2014; Grillmair 2014; Lee et al. 2015, and references therein). Searches using the early Pan-STARRS and VST ATLAS survey data were less successful, revealing only two new satellites thus far (Belokurov et al. 2014; Laevens et al. 2015). More recently however, the publicly-accessible Dark Energy Survey (DES hereafter; The Dark Energy Survey Collaboration 2005)

data has been used by two independent groups to find at least another 9 satellites (Koposov et al. 2015; The DES Collaboration et al. 2015). The wide-field imaging capabilities of the DECam have also been exploited by a number of smaller-scale surveys of the Milky Way halo, increasing the tally of Galactic satellites at a breakneck pace (Kim & Jerjen 2015a; Kim et al. 2015b,c; Martin et al. 2015). Many of these latest discoveries are remarkably feeble, fainter than most known systems, rightfully earning the name of ‘ultra-faint’ satellites.

As more ultra-faint satellites (UFS) have been discovered, complications have arisen in trying to accurately classify them. A tenuous overlap between the effective radii and absolute magnitudes of faint globular clusters and ultra-faint dwarf galaxies has emerged. It is now crystal clear, the morphology of ultra-faint systems near the *valley of ambiguity* cannot be classified from photometry alone (Gilmore et al. 2007). Kinematics and chemistry are required to distinguish between these classifications. A large dispersion in overall metallicity is representative of extended star formation in a dwarf galaxy-like environment that is massive enough to retain supernova ejecta, providing a key diagnostic for distinguishing globular clusters and dwarf galaxies (e.g., Willman & Strader 2012). Indeed, spectroscopy is essential for a large number of confirmed members in order to precisely measure velocity and chemical dispersions, estimate the dark matter content, and explore the star formation histories of these ancient systems (e.g., Kirby et al. 2011; Tollerud et al. 2012).

The UFSs have been the focus of attention of Galactic archaeologists world wide for less than a decade. Worryingly, during this short history, many of their spectroscopically determined properties have continued to evolve. For example, the early studies of the Boötes 1 dwarf spheroidal reported a velocity dispersion as high as 6.5 km s^{-1} (Muñoz et al. 2006; Martin et al. 2007). However, an independent and novel study by Koposov et al. (2011) revealed that the dwarf’s internal kinematics is potentially dominated by a stellar population with a velocity dispersion as low as 2.4 km s^{-1} . Similarly, for the Segue 2 satellite, Belokurov et al. (2009) gave an estimate of 3.4 km s^{-1} and a warning of a potential contamination from the surrounding Tri-And stream. In fact, Kirby et al. (2013) later showed the velocity of Segue 2 is consistent with zero, thus ruling out the presence of any significant amount of dark matter in the system. Undoubtedly, robust uncertainties on individual stellar velocity measurements are paramount to accurate characterization of the kinematics of these systems. Furthermore, inferences are susceptible to low-number statistics, as well as contamination from foreground stars or binary systems.

The Gaia-ESO Survey (Gilmore et al. 2012; Randich et al. 2013) has been obtaining high-resolution spectra using the Very Large Telescope (VLT) in Chile since January 2012. The primary scientific goal of the Gaia-ESO Survey is to characterise the major constituents of the Galaxy, and to understand these components in the context of the Milky Way’s formation history. To that end, more than 10^5 Milky Way stars are homogeneously targeted as part of the Gaia-ESO Survey, including all major structural components: open and globular clusters,

the disk, bulge, and the halo. Understanding the role of ultra-faint satellites is indeed important in this context, as they inform us of star formation in isolated environments as well as the accretion history of the Galaxy.

Here we report on Gaia-ESO Survey observations of two of the recently discovered ultra-faint dwarf satellites: Reticulum 2 and Horologium 1. Reticulum 2 is a mere $\sim 30 \text{ kpc}$ away towards the Large Magellanic Cloud (LMC) with a $M_v = -2.7 \pm 0.1$, and is suspected to be very dark matter-dominated. Indeed, Reticulum 2 is of particular scientific interest given the recently reported detection of dark matter annihilation (Geringer-Sameth et al. 2015; The Fermi-LAT Collaboration et al. 2015). Horologium 1, also located towards the LMC, is more distant at 79 kpc but given somewhat brighter luminosity of $M_v = -3.4 \pm 0.1$ and a visible giant branch, spectroscopy of candidate red giant branch (RGB) stars is accessible from the VLT in a standard Gaia-ESO Survey observing block. While our primary goal is to establish the true nature of these faint stellar systems by gauging the amount dark matter they might contain, we also intend to test the hypothesis that the dwarfs have once been part of the Magellanic group.

We outline the target selection and the data that we will subsequently analyse in Section 2. A detailed description of our analysis is outlined in Section 3. We discuss the interpretations of our results in Section 4.

2. OBSERVATIONS

The data were obtained in $0.8''$ seeing using the FLAMES spectrograph (Pasquini et al. 2002) on the 8.2 m Very Large Telescope (VLT/UT2) at Cerro Paranal, Chile. Candidate members of both satellites were targeted using otherwise unallocated Milky Way fibres on February 6 and March 8-10, 2015 as part of the ongoing Gaia-ESO Survey (ESO Programme 188.B-3002 Gilmore et al. 2012; Randich et al. 2013). In the field `GES_MW_033542.540254` 109 fibers were allocated to science targets, with 25 allocated to Reticulum 2 candidates, and the rest allocated to standard Gaia-ESO Milky Way targets. In the field `GES_MW_025532.540711`, the total number of allocated fibers was 107, with 18 fibers assigned to Horologium 1 candidates. The HR10 and HR21 setups were employed, providing high-resolution ($\mathcal{R} \sim 19800$ and 16200^1) spectra in wavelength regions of $5334\text{--}5611 \text{ \AA}$ and $8475\text{--}8982 \text{ \AA}$, respectively.

The candidate satellite members were selected using a broad color-magnitude mask based on the best fitting isochrone and distance modulus from Koposov et al. (2015) (hereafter K15). We also required that the targets were located within $10 - 15'$ on the sky from the satellite center. Figure 1 shows the color-magnitude distribution of stars near the center of both systems. Candidates that were observed spectroscopically are highlighted, as well as those which we later confirmed to be members.

The data were reduced using standard procedures performed for all other Gaia-ESO Survey GIRAFFE observations. This process includes bias correction, flat-fielding, object extraction, sky subtraction, scattered

¹ Note however that the resolving power and sensitivity of the GIRAFFE instrument has been recently improved due to refocusing, see <http://eso.org/sci/publications/announcements/sciann15013.html>

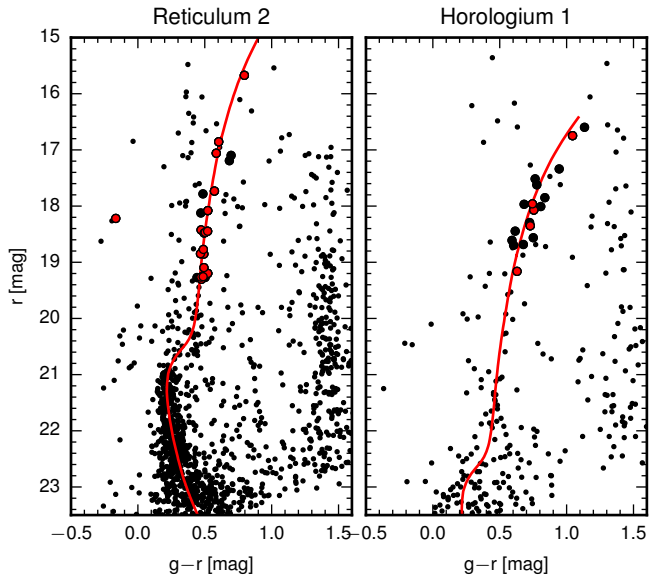


FIG. 1.— Color-magnitude distribution of stars near the centers of Reticulum 2 and Horologium 1 satellites. Large black circles indicate candidates that were observed with VLT/GIRAFFE, and the red symbols are those we later confirmed to be members of each system. Each panel shows a 12.5 Gyr PARSEC isochrone Bressan et al. (2012) with a $[\text{Fe}/\text{H}] = -2$ that has been shifted according to the distance modulus from K15.

light correction, and wavelength calibration. The spectra are then corrected for barycentric motion and re-sampled onto a common wavelength scale (Lewis et al. 2015). Generally the mean signal-to-noise (S/N) ratio per pixel is quite low: 5/13 for Reticulum 2 candidates in HR10/HR21 respectively, and 4/10 for the Horologium 1 candidates. However the brightest confirmed members of either satellite (Section 3.3) have S/N ratios of 26/62 (Reti 4; HR10/HR21) and 10/28 per pixel (Horo 10; see Figure 2).

3. ANALYSIS

3.1. Kinematics

The velocity analysis has been performed using standard Gaia-ESO Survey radial velocity (RV) pipeline. Although the full details of this pipeline will be presented in Lewis et al. (2015), here we outline the principle components. The algorithm is based on a direct pixel-fitting procedure implemented by Koposov et al. (2011) (see also Koleva et al. 2009; Walker et al. 2015a), and employs the PHOENIX library of model stellar spectra (Husser et al. 2013). All of the observed spectra are fitted (using a χ^2 metric) by model templates that are interpolated from the spectral library, and the continuum is modelled by a high-degree polynomial. The maximum likelihood point is found by using Nelder-Mead algorithm (Nelder & Mead 1965), using several starting points to avoid being trapped in local maxima. The location of the maximum likelihood (χ^2 minimum) and the Hessian of the likelihood surface are used to provide the best-fit velocity, errors and estimates of the stellar atmospheric parameters.

The crucial ingredient in correctly extracting the kinematics of ultra-faint satellites is a proper understanding of the uncertainties of RV measurements (see e.g., Geha et al. 2009; Koposov et al. 2011). Because the Gaia-ESO

Survey has already observed many thousands of stars, some of them repeatedly and with different instrument configurations, our experience with the Survey provide us with a very good understanding of the RV precision achievable. For this paper, however, we focus only on data in just two Gaia-ESO Milky Way fields: those with Horologium 1 and Reticulum 2 candidates.

In addition to the standard data processing steps performed for the Gaia-ESO Survey, there are three subtle points that are important for this study:

- *Spectral covariance.* The standard Gaia-ESO reduction pipeline rebins the spectra to a common wavelength mapping with a fixed step size. For HR10 the common wavelength scale extends from 5334-5611Å and for HR21 the boundaries are 8475-8982Å, both with a spacing of 0.05Å. While convenient for some analyses, the rebinning procedure introduces correlated noise/covariance in the spectra and reduces the effective information content of the spectra. For example, the rebinned HR21 spectra has 10141 pixels, the rebinned HR10 spectra has 5541 pixels, while the original spectra are just 4096 pixels. We can account for this correlation by modelling the spectra with the full covariance matrix, or approximate it. Our tests found that if we fit the spectra using the full covariance matrix of the data and the posterior/likelihood is properly behaved (e.g., uni-modal and close to a Gaussian), then the effect of pixel covariance is equivalent to scaling the errors by a fixed constant: 1.5 for HR10, 2.0 for HR21. These numbers are approximately equal to the ratio of rebinned and original pixels. We adopt this scaling throughout the rest of our analysis. See the end of this section for the verification of the results.
- *Systematic error floor.* It is well-known that although the formal RV precision derived from cross-correlation or pixel-fitting methods can be almost arbitrarily small for sufficiently high S/N spectra, the actual precision achievable with most spectrographs is generally limited by systematic effects. This includes instrument flexures, uncertainties in the wavelength calibrations, Line Spread Function (LSF) variation/asymmetry and template mismatches. This systematic component has to be included in the total error budget. We have found this systematic error to be around 300 m s^{-1} from large numbers of Gaia-ESO Milky Way spectra. It is important to note that this systematic component is not expected to be present when comparing RVs obtained from spectra using the same setup in sequential exposures, but it becomes important when comparing RVs from different nights, or between HR10 and HR21 setups. We include this systematic error floor in suitable comparisons hereafter.
- *RV offset between HR10 and HR21.* Over the course of the Gaia-ESO Survey, it has been discovered that there is a small systematic offset of 400 m s^{-1} between the RVs measured in the HR10 and HR21 setups. The cause of this offset is not

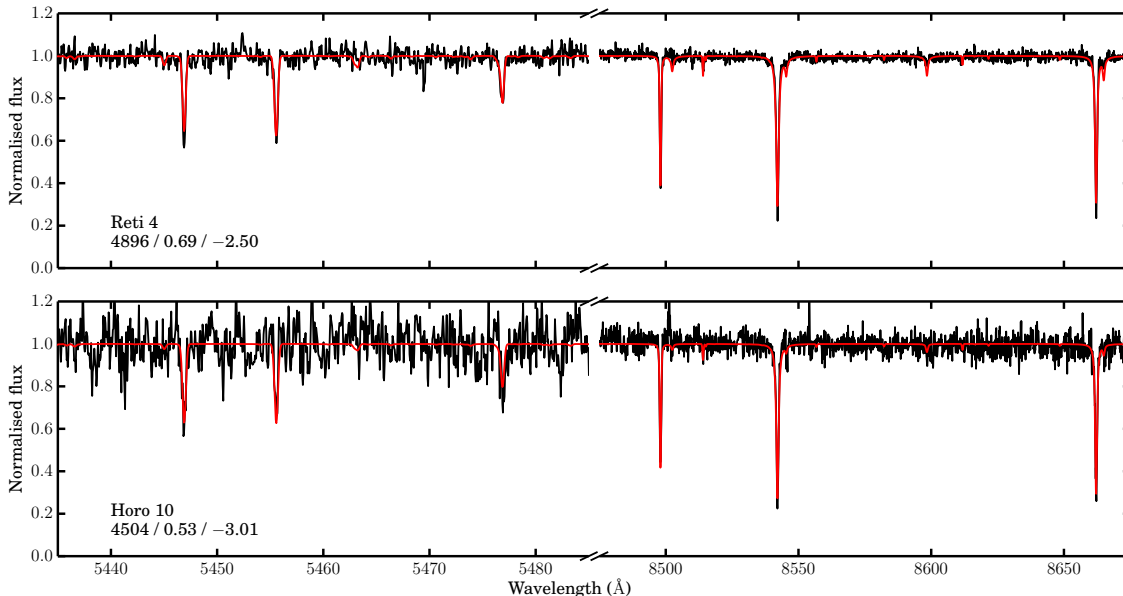


FIG. 2.— An example showing the observed (black) and maximum a posteriori model (red) spectra for a confirmed Reticulum 2 (top) and Horologium 1 (bottom) member. These spectra have the highest S/N ratio of confirmed members in each system.

well-established yet. This correction was applied to the radial velocities (the HR21 velocities have been shifted by -400 m s^{-1}).

After applying the aforementioned corrections, we can confirm whether the RVs measured in repeated exposures match within the precision quoted by our error bars. To test this we have collated all the spectra in the `GES_MW_033542_540254` and `GES_MW_025532_540711` fields (i.e., including both standard Gaia-ESO targets and possible satellite member stars). The top panel of Figure 3 shows the distribution of velocity differences ($V_1 - V_2$) scaled by the RV error ($\sqrt{\sigma(V_1)^2 + \sigma(V_2)^2}$) for repeated HR10 exposures. The middle panel of the figure shows the same for the HR21 setup. The bottom panel shows the distribution of normalised velocity differences for HR10 exposures versus HR21. In all the panels the red curve shows a standard normal distribution with zero mean and unit variance. In all cases the distributions are indeed well described by Gaussians, confirming that our error model provides a correct description of the velocity uncertainties.

The final radial velocities for all the observed Reticulum 2 and Horologium 1 candidate members are provided in Table 2 and refer to the weighted means of the HR10 and HR21 measurements and take into account all the error-terms mentioned above.

3.2. Chemistry

We used a generative model to infer the stellar parameters for all stars. The model is described as follows. For a given set of stellar parameters $\omega = \{T_{\text{eff}}, \log g, [\text{Fe}/\text{H}], [\alpha/\text{Fe}]\}$ we first produce a flux-normalised synthetic spectrum $S(\lambda, \omega)$ at wavelengths λ by interpolating spectra from a surrounding grid. The synthetic spectra were calculated as per the AMBRE grid (see de Laverny et al. 2012, for details). This high-resolution ($\mathcal{R} > 300,000$) grid was synthesised specifically for the Gaia-ESO Survey using Turbospectrum (Al-

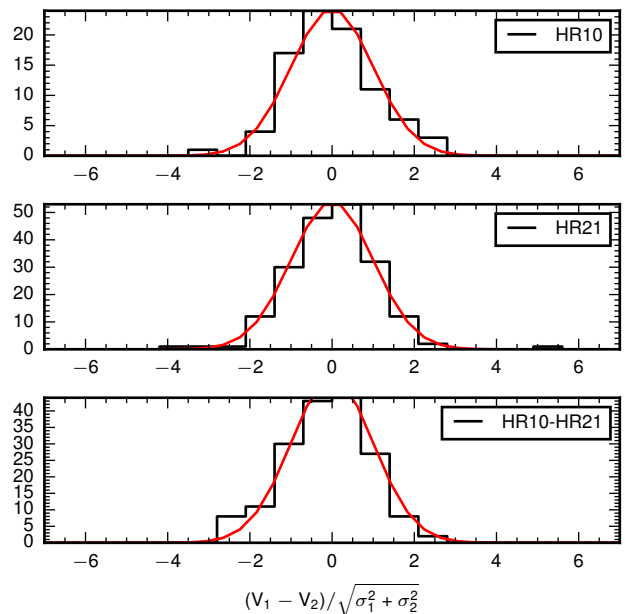


FIG. 3.— The results of radial velocity precision tests done using repeated observations. The three panels show the distribution of the RV difference normalised by their errors as measured in the HR10 (top panel), HR21 (middle panel) and HR10-HR21 configurations (bottom panel). These tests demonstrate that our error model is correct, as the distributions very closely resemble a normal distribution with zero-mean and unit variance shown by red curves on the panels.

varez & Plez 1998; Plez 2012), the MARCS (Gustafsson et al. 2008) model atmospheres and the Gaia-ESO Survey line list (Ruffoni et al. 2014; Heiter et al. 2015, V5 for atoms and molecules). The grid includes effective temperatures from 3000 K to 8000 K, and surface gravities from $\log g = 0$ to 5. Metallicities extend from as low as $[\text{Fe}/\text{H}] = -5$ with 1 dex steps until $[\text{Fe}/\text{H}] = -3$ and 0.25 dex steps thereafter, extending past solar metallicity.

In the metallicity range applicable for this study, $[\alpha/\text{Fe}]$ ratios vary between 0.0 and +0.8 at steps of 0.2 dex. We redshift our interpolated spectrum by velocity V such that the normalised synthetic flux at an observed point λ is given by $S\left(\lambda\left[1 + \frac{V}{c}\right], \omega\right)$, where c is the speed of light. The observed continuum is modelled as a low-order polynomial with coefficients b_j that enters multiplicatively:

$$M(\lambda, \omega, v, \{b\}) = \sum_{j=0}^{N-1} b_{\text{channel},j} \lambda^j \times S\left(\lambda\left[1 + \frac{V}{c}\right], \omega\right) \quad (1)$$

The continuum in each observed channel (HR10 and HR21) are modelled separately. In practice we found a first-order polynomial to sufficiently represent the continuum in each channel. Lastly, we convolve the model spectrum with a Gaussian LSF (with free parameter \mathcal{R}) to match the resolving power in each channel, and resample the model spectrum to the observed pixels $\{\lambda\}$. Although the spectral resolution \mathcal{R} in each channel is reasonably well-known, recent refocusing of the GIRAFFE spectrograph has improved the quoted spectral resolution. For this reason we chose to include the spectral resolution \mathcal{R} as a nuisance parameter with reasonable priors and marginalise them away. The prior on spectral resolution was uniformly distributed to within $\pm 30\%$ of $\mathcal{R} = 16200$ and 19800 for the HR10 and HR21 setups respectively. After convolution with the LSF, binning to the observed pixels $\{\lambda\}$ and assuming Gaussian error σ_i , the probability distribution $p(F_i|\lambda_i, \sigma_i, \omega, V, \{b\}, \{\mathcal{R}\})$ for the observed spectral flux F_i is:

$$p(F_i|\lambda_i, \sigma_i, \omega, V, \{b\}, \{\mathcal{R}\}) = \frac{1}{\sqrt{2\pi\sigma_i^2}} \exp\left(-\frac{[F_i - M_i]^2}{2\sigma_i^2}\right). \quad (2)$$

Under the implied assumption that the data are independently drawn, the likelihood of observing the data D , given our model, is found by the product of individual probabilities:

$$\mathcal{L} = \prod_{i=1}^N p(F_i|\lambda_i, \sigma_i, \omega, V, \{b\}, \{\mathcal{R}\}) \quad (3)$$

and the probability \mathcal{P} of observing the data is proportional up to a constant such that:

$$\begin{aligned} \mathcal{P} &\propto \mathcal{L}(D|\theta) \times \mathcal{P}r(\theta) \\ \ln \mathcal{P} &= \ln \mathcal{L}(D|\theta) + \ln \mathcal{P}r(\theta) \end{aligned} \quad (4)$$

where $\mathcal{P}r(\theta)$ is the prior probability on the model parameters θ .

In practice we found that the spectral range of our data were not particularly informative of the effective temperature T_{eff} for very metal-poor stars. For these stars the data were prone to favour unphysically cool super giant stars of extremely low metallicity. We did not find the same effect for more metal-rich stars, where there are sufficient neutral and ionising transitions present to accurately constrain the stellar parameters. Given most of our candidates are indeed metal-poor, we found it prudent to fix the effective temperature using the DES pho-

tometry and a colour-temperature relation². We found this had no significant impact on our posteriors for the foreground dwarfs – where the spectra are indeed informative of effective temperature – and ultimately did not substantially alter our inferred metallicity dispersion for either satellite. Only the mean satellite metallicities were affected. The uncertainties in effective temperature listed in Table 2 were calculated by propagating the DES photometric uncertainties with the intrinsic uncertainty in the colour-temperature relation. Thus, our forward model is subject to our photometric temperatures and has only 10 parameters: $\log g$, $[\text{Fe}/\text{H}]$, $[\alpha/\text{Fe}]$, V , the resolving powers $\mathcal{R}_{\text{HR10}}$ and $\mathcal{R}_{\text{HR21}}$, as well as two continuum coefficients in each channel.

The initial model parameters V and ω (modulo T_{eff}) were estimated by performing a coarse normalisation of the data and cross-correlating it against the de Laverny et al. (2012) grid. Although we have fixed T_{eff} and previously determined V (see Section 3.1) we still carried out the cross-correlation to yield a reliable initial estimate of $\log g$, $[\text{Fe}/\text{H}]$ and $[\alpha/\text{Fe}]$. We also used the synthetic flux at the grid point with the peak cross-correlation coefficient to subsequently estimate the normalisation coefficients $\{b\}$. We numerically optimised the negative log-probability $-\ln \mathcal{P}$ from the initial point using the Nelder-Mead algorithm (Nelder & Mead 1965). Following optimisation, we sampled the resulting posterior using the affine-invariant Markov Chain Monte Carlo (MCMC) sampler introduced by Goodman & Weare (2010) and implemented by Foreman-Mackey et al. (2013). In all cases at least 200 walkers were used to explore the parameter space for more than 2500 steps ($\geq 5 \times 10^5$ probability evaluations) to burn-in the sampler. These probability calls were discarded and the chains were reset before production sampling began. We tested our MCMC analyses for convergence by examining the auto-correlation times (e.g., ensuring high effective sample numbers per parameter) and the mean acceptance fractions over time. We also re-ran a subset of our analyses with many more evaluations (for both burn-in and production), verifying that there was no change to the resulting posteriors.

We list the photometric effective temperatures and other inferred stellar parameters (given the model and effective temperature) in Table 2. The middle panels of Figure 4 show the inferred surface gravities for all candidates. Our confirmed members agree well with the metal-poor isochrone shown. This is particularly true for the higher-quality Reticulum 2 data, with the possible exception of the metal-poor giant Reti 4, where the $\log g$ seems quite low. Although this star has the highest S/N ratio in our sample, metal-poor super giant stars are very challenging to model from an astrophysical perspective. Nevertheless, the marginalised posterior metallicity distribution for Reti 4 agrees excellently with stars further down the giant branch of lower S/N ratios. Table 2 also lists the reduced χ^2 values of our spectral fits. In general the values are quite close to 1. However due to lower S/N and imperfect sky-subtraction in the Horologium 1 data, the $\chi^2/\text{d.o.f.}$ values for those candidates are slightly higher.

² The colour-temperature relation was defined by fitting the relation between DES g–r colors and effective temperature from SEGUE (Lee et al. 2008).

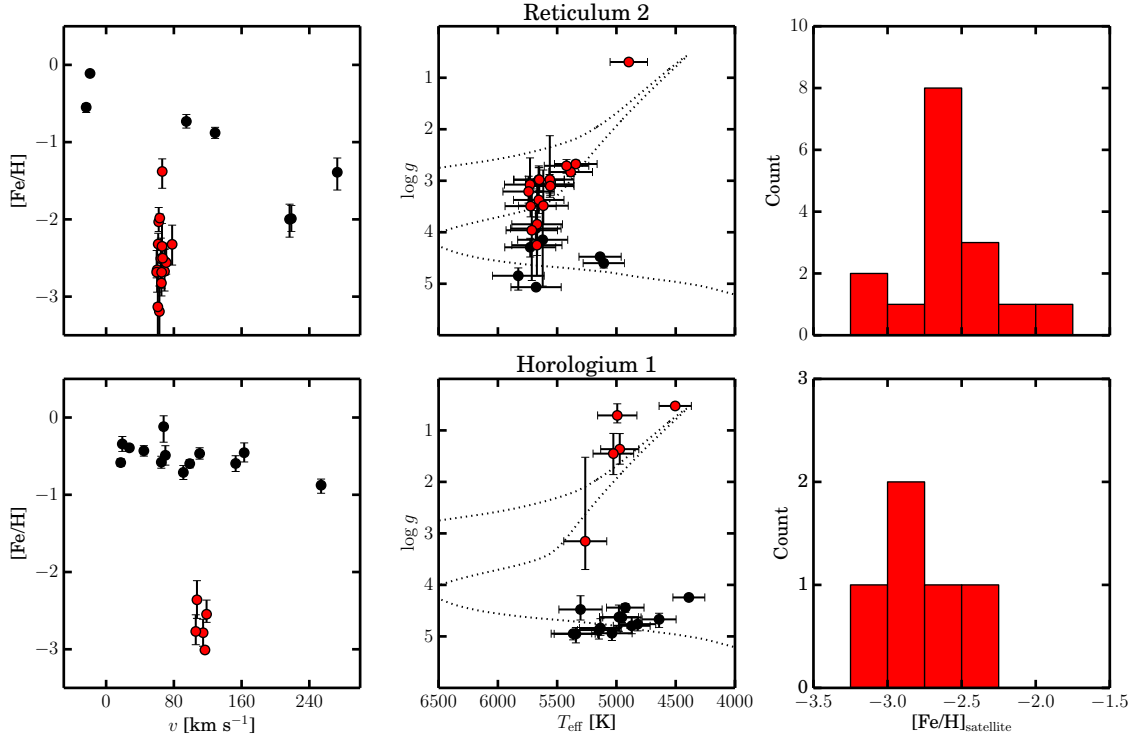


FIG. 4.— Inferred radial velocities and stellar parameters for all Reticulum 2 (top) and Horologium 1 (bottom) candidates. Confirmed members (marked in red) cleanly separate from foreground contaminants in $v - [\text{Fe}/\text{H}]$ space (left). Photometric effective temperatures (see text) and spectroscopically-derived surface gravities are shown in the middle panel, overlaid upon a 12 Gyr PARSEC isochrone (Bressan et al. 2012) with a metallicity of $[\text{Fe}/\text{H}] = -2$. Histograms of the maximum a posteriori metallicities of confirmed members are shown in the right-hand panels.

Our radial velocity determination for Reti 22 confirms it as a horizontal branch member of Reticulum 2 (see Section 3.3). However, the photometric temperature estimate of 8468^{+306}_{-295} K prohibited us from inferring other stellar parameters for this star, as it is hotter than the boundary (8000 K) of the spectral grid.

Two members of Reticulum 2 have maximum a posteriori (MAP) $\log g$ values that are consistent with being a dwarf (Figure 4). This is inconsistent with the photometry, since the main-sequence is too faint for us to target with standard exposure times for Gaia-ESO Survey Milky Way fields. However, the negative uncertainties on $\log g$ for these two Reticulum 2 members are considerably large, making them deviate from the giant branch by only 1 to 1.5σ . As a test we constrained the prior on surface gravity to be uninformative between $\log g \in [-0.5, 4.0]$, forcing the star to be a giant/sub-giant, but we found no statistically significant difference in the marginalized posterior metallicity distribution.

Similarly while all confirmed Horologium 1 stars are giants, and the foreground contaminants are clearly dwarfs, one star (Horo 17) has a very low S/N and consequently has an extremely large negative uncertainty in $\log g$. While the posterior demonstrates the star is not a dwarf, we cannot place its precise location on the giant branch.

Our inferred $[\alpha/\text{Fe}]$ abundance ratios are informative, even with their large uncertainties. Unsurprisingly, we found the $[\alpha/\text{Fe}]$ ratio to be strongly correlated with other stellar parameters, particularly $[\text{Fe}/\text{H}]$. We find the foreground contaminants to largely follow the well-studied Milky Way trend in $[\text{Fe}/\text{H}] - [\alpha/\text{Fe}]$. All the

TABLE 1
SUMMARY PROPERTIES OF RETICULUM 2 AND HOROLOGIUM 1

	Reticulum 2	Horologium 1
α (J2000) [deg]	53.9256	43.8820
δ (J2000) [deg]	-54.0592	-54.1188
Distance [kpc]	30	79
M_V	-2.7 ± 0.1	-3.4 ± 0.1
Ellipticity	$0.59^{+0.02}_{-0.03}$	< 0.28
$r_{1/2}$ [arcmin]	$3.64^{+0.21}_{-0.12}$	$1.31^{+0.19}_{-0.14}$
$r_{1/2}$ [pc]	$32^{+1.9}_{-1.1}$	$30^{+4.4}_{-3.3}$
V_{hel} [km s $^{-1}$]	$64.7^{+1.3}_{-0.8}$	$112.8^{+2.5}_{-2.6}$
σ (V) [km s $^{-1}$]	$3.22^{+1.64}_{-0.49}$	$4.9^{+2.8}_{-0.9}$
Mass($< r_{1/2}$) [M_\odot]	$2.35^{+4.71}_{-0.13} \times 10^5$	$5.5^{+11.3}_{-1.0} \times 10^5$
M/L_V [M_\odot/L_\odot]	479^{+904}_{-51}	570^{+1154}_{-112}
$[\text{Fe}/\text{H}]$	$-2.46^{+0.09}_{-0.1}$	$-2.76^{+0.1}_{-0.1}$
σ ($[\text{Fe}/\text{H}]$) [dex]	$0.29^{+0.13}_{-0.05}$	$0.17^{+0.2}_{-0.03}$
$[\alpha/\text{Fe}]$	0.40 ± 0.04	0.30 ± 0.07

NOTE. — Properties above the horizontal separator were adopted from Koposov et al. (2015). Those below the separator were determined in this study.

confirmed members in Reticulum 2 and Horologium 1 appear to have at least $[\alpha/\text{Fe}] \gtrsim +0.2$, with an point estimate (assumed δ -function distribution) of $[\alpha/\text{Fe}] \approx +0.4$ in Reticulum 2 and $\approx +0.3$ in Horologium 1.

3.3. Joint modeling of satellites kinematics and chemistry

Having measured the chemical abundances and radial velocities of individual stars in two satellites the next

TABLE 2
POSITIONS, VELOCITIES, STELLAR PARAMETERS AND MEMBERSHIP FOR RETICULUM 2 AND HOROLOGIUM 1 CANDIDATES

Object	α (J2000) [deg]	δ (J2000) [deg]	g [mag]	V_{hel} [km s ⁻¹]	T_{eff} [K]	$\log g$	[Fe/H]	[α /Fe]	χ^2_{red}	Member?
Reticulum 2										
Reti 0	53.9424	-54.1260	19.27	218.5 \pm 1.1	5680 ⁺²¹⁷ ₋₂₀₉	3.93 ^{+0.35} _{-0.33}	-1.99 ^{+0.17} _{-0.17}	0.55 ^{+0.17} _{-0.19}	1.11	
Reti 1	53.8133	-54.1452	19.78	78.9 \pm 1.8	5714 ⁺²²¹ ₋₂₁₃	3.96 ^{+0.80} _{-0.98}	-2.32 ^{+0.27} _{-0.25}	0.61 ^{+0.14} _{-0.22}	0.96	Yes
Reti 2	53.8072	-54.0824	19.74	60.0 \pm 2.1	5729 ⁺²¹¹ ₋₂₀₄	3.07 ^{+0.43} _{-0.32}	-2.65 ^{+0.29} _{-0.32}	0.45 ^{+0.24} _{-0.28}	0.95	Yes
Reti 3	53.9045	-54.0670	18.60	65.6 \pm 0.9	5558 ⁺²⁰⁴ ₋₁₉₇	3.10 ^{+0.17} _{-0.18}	-2.82 ^{+0.17} _{-0.12}	0.65 ^{+0.11} _{-0.17}	1.00	Yes
Reti 4	53.8494	-54.0687	16.47	66.3 \pm 0.2	4896 ⁺¹⁶⁰ ₋₁₅₅	0.69 ^{+0.02} _{-0.02}	-2.50 ^{+0.02} _{-0.02}	0.23 ^{+0.01} _{-0.01}	1.43	Yes
Reti 5	53.8374	-54.0633	18.97	69.1 \pm 1.0	5655 ⁺²¹⁶ ₋₂₀₈	3.37 ^{+0.63} _{-0.26}	-2.54 ^{+0.18} _{-0.16}	0.59 ^{+0.14} _{-0.22}	1.03	Yes
Reti 6	53.7260	-54.0994	18.97	70.8 \pm 1.1	5617 ⁺²¹⁴ ₋₂₀₆	3.48 ^{+0.69} _{-0.36}	-2.56 ^{+0.15} _{-0.25}	0.14 ^{+0.20} _{-0.11}	0.91	Yes
Reti 7	53.7399	-54.0920	18.97	61.9 \pm 0.8	5564 ⁺²⁰⁷ ₋₁₉₉	3.07 ^{+0.19} _{-0.17}	-2.03 ^{+0.12} _{-0.19}	0.39 ^{+0.17} _{-0.15}	1.05	Yes
Reti 8	53.7605	-54.0650	19.26	65.4 \pm 1.8	5669 ⁺²¹⁷ ₋₂₀₉	3.84 ^{+0.89} _{-0.61}	-2.51 ^{+0.27} _{-0.26}	0.29 ^{+0.30} _{-0.22}	0.91	Yes
Reti 9	53.8209	-54.0675	19.74	62.9 \pm 3.7	5671 ⁺²¹⁶ ₋₂₀₈	4.25 ^{+0.55} _{-0.60}	-3.13 ^{+0.39} _{-0.45}	0.22 ^{+0.30} _{-0.20}	1.44	Yes
Reti 10	53.8540	-54.0418	19.72	65.6 \pm 1.2	5562 ⁺²⁰⁷ ₋₂₀₀	2.98 ^{+0.85} _{-0.34}	-1.38 ^{+0.22} _{-0.16}	0.42 ^{+0.20} _{-0.22}	0.98	Yes?
Reti 11	53.7986	-54.0560	19.35	68.2 \pm 1.7	5651 ⁺²¹⁷ ₋₂₁₀	2.98 ^{+0.24} _{-0.22}	-2.67 ^{+0.25} _{-0.28}	0.39 ^{+0.26} _{-0.26}	1.17	Yes
Reti 12	53.7896	-54.0416	18.27	94.7 \pm 0.4	5678 ⁺²¹⁶ ₋₂₀₈	5.07 ^{+0.71} _{-0.01}	-0.73 ^{+0.09} _{-0.09}	0.31 ^{+0.07} _{-0.06}	1.02	
Reti 13	54.0980	-54.0885	19.77	220.3 \pm 2.0	5622 ⁺²⁰⁷ ₋₂₀₀	4.15 ^{+0.77} _{-0.90}	-2.00 ^{+0.23} _{-0.19}	0.53 ^{+0.17} _{-0.25}	1.04	
Reti 14	54.0074	-54.0681	19.59	63.4 \pm 1.7	5655 ⁺²¹⁸ ₋₂₁₀	2.98 ^{+0.27} _{-0.25}	-3.19 ^{+0.31} _{-0.33}	0.46 ^{+0.23} _{-0.27}	1.14	Yes
Reti 15	53.9502	-54.0638	18.30	63.5 \pm 0.5	5421 ⁺¹⁹¹ ₋₁₈₅	2.71 ^{+0.12} _{-0.14}	-1.98 ^{+0.06} _{-0.05}	0.47 ^{+0.06} _{-0.07}	1.11	Yes
Reti 16	53.9582	-54.0559	19.71	292.1 \pm 1.3	5828 ⁺²²³ ₋₂₂₀	4.84 ^{+0.15} _{-0.26}	-1.39 ^{+0.23} _{-0.21}	0.54 ^{+0.17} _{-0.23}	1.06	
Reti 17	53.9845	-54.0545	18.90	65.9 \pm 1.2	5724 ⁺²¹¹ ₋₁₈₃	3.49 ^{+0.21} _{-0.07}	-2.68 ^{+0.30} _{-0.04}	0.22 ^{+0.17} _{-0.16}	1.09	Yes
Reti 18	54.0323	-54.0432	17.46	61.4 \pm 0.4	5343 ⁺¹⁸³ ₋₁₇₇	2.67 ^{+0.07} _{-0.06}	-2.32 ^{+0.04} _{-0.14}	0.42 ^{+0.16} _{-0.02}	1.05	Yes
Reti 19	53.9923	-54.0346	19.32	65.0 \pm 1.4	5741 ⁺²²¹ ₋₂₁₂	3.21 ^{+0.30} _{-0.22}	-2.35 ^{+0.23} _{-0.30}	0.22 ^{+0.29} _{-0.22}	1.06	Yes
Reti 20	54.0163	-54.0073	17.79	-23.6 \pm 0.3	5107 ⁺¹⁷⁷ ₋₁₇₁	4.60 ^{+0.07} _{-0.09}	-0.55 ^{+0.07} _{-0.05}	0.19 ^{+0.01} _{-0.06}	1.06	
Reti 21	54.0952	-53.9987	18.59	128.9 \pm 0.5	5727 ⁺²¹⁹ ₋₂₁₉	4.29 ^{+0.17} _{-0.19}	-0.88 ^{+0.07} _{-0.07}	-0.01 ^{+0.06} _{-0.06}	0.97	
Reti 22	54.0779	-53.9625	18.05	61.6 \pm 2.6	8468 ⁺³⁰⁶ ₋₂₉₅	Yes
Reti 23	53.8798	-54.0300	17.64	59.6 \pm 0.5	5386 ⁺¹⁸⁷ ₋₁₈₁	2.83 ^{+0.09} _{-0.09}	-2.68 ^{+0.07} _{-0.28}	0.47 ^{+0.30} _{-0.07}	1.16	Yes
Reti 24	53.9127	-53.9323	17.88	-19.2 \pm 0.3	5138 ⁺¹⁸¹ ₋₁₇₅	4.48 ^{+0.06} _{-0.05}	-0.11 ^{+0.03} _{-0.03}	0.09 ^{+0.02} _{-0.02}	1.00	
Horologium 1										
Horo 0	43.9692	-54.3117	18.81	110.6 \pm 0.4	5135 ⁺¹⁷⁹ ₋₁₇₃	4.84 ^{+0.18} _{-0.15}	-0.47 ^{+0.07} _{-0.08}	0.30 ^{+0.06} _{-0.06}	2.01	
Horo 1	44.0306	-54.2768	18.28	254.2 \pm 0.2	4640 ⁺¹⁴⁶ ₋₁₄₁	4.67 ^{+0.12} _{-0.16}	-0.88 ^{+0.10} _{-0.08}	0.29 ^{+0.04} _{-0.04}	1.58	
Horo 2	43.8105	-54.2267	19.20	152.6 \pm 0.8	5365 ⁺¹⁸⁹ ₋₁₈₂	4.95 ^{+0.05} _{-0.12}	-0.59 ^{+0.10} _{-0.10}	0.38 ^{+0.10} _{-0.11}	2.23	
Horo 3	43.6503	-54.1802	17.73	27.5 \pm 0.1	4389 ⁺¹³⁷ ₋₁₃₂	4.24 ^{+0.05} _{-0.02}	-0.39 ^{+0.02} _{-0.03}	0.21 ^{+0.03} _{-0.01}	2.03	
Horo 5	44.1126	-54.2174	17.79	64.8 \pm 0.5	5038 ⁺¹⁷³ ₋₁₆₈	4.94 ^{+0.07} _{-0.14}	-0.58 ^{+0.08} _{-0.08}	0.29 ^{+0.07} _{-0.07}	1.58	
Horo 6	44.1567	-54.1941	19.06	91.2 \pm 0.9	4871 ⁺¹⁵⁸ ₋₁₅₃	4.79 ^{+0.16} _{-0.15}	-0.71 ^{+0.09} _{-0.09}	0.38 ^{+0.05} _{-0.08}	2.22	
Horo 7	44.0076	-54.1986	19.30	163.1 \pm 1.0	5148 ⁺¹⁸² ₋₁₇₆	4.88 ^{+0.10} _{-0.17}	-0.46 ^{+0.12} _{-0.13}	0.39 ^{+0.12} _{-0.10}	1.53	
Horo 9	43.9179	-54.1353	18.71	118.5 \pm 0.5	4993 ⁺¹⁶⁸ ₋₁₆₃	0.71 ^{+0.23} _{-0.15}	-2.55 ^{+0.11} _{-0.18}	0.35 ^{+0.17} _{-0.14}	1.97	Yes
Horo 10	43.8967	-54.1122	19.31	116.6 \pm 0.1	4504 ⁺¹³⁸ ₋₁₃₄	0.53 ^{+0.04} _{-0.02}	-3.01 ^{+0.02} _{-0.03}	0.36 ^{+0.03} _{-0.03}	1.83	Yes
Horo 11	43.9699	-54.0877	18.83	114.6 \pm 0.7	4972 ⁺¹⁶³ ₋₁₅₈	1.36 ^{+0.30} _{-0.29}	-2.79 ^{+0.17} _{-0.17}	0.35 ^{+0.19} _{-0.18}	2.24	Yes
Horo 15	43.8912	-54.0939	19.08	105.6 \pm 1.0	5026 ⁺¹⁷⁴ ₋₁₆₈	1.45 ^{+0.39} _{-0.41}	-2.77 ^{+0.17} _{-0.22}	0.15 ^{+0.21} _{-0.11}	2.02	Yes
Horo 17	43.8719	-54.0727	18.65	108.1 \pm 1.9	5263 ⁺¹⁸⁴ ₋₁₇₈	3.15 ^{+1.63} _{-0.55}	-2.36 ^{+0.24} _{-0.25}	0.18 ^{+0.27} _{-0.17}	2.03	Yes
Horo 18	43.8497	-54.0445	18.40	17.1 \pm 0.2	4925 ⁺¹⁶⁰ ₋₁₅₅	4.44 ^{+0.08} _{-0.09}	-0.58 ^{+0.05} _{-0.05}	0.16 ^{+0.05} _{-0.04}	4.25	
Horo 19	43.8867	-53.9968	19.79	18.7 \pm 0.6	5303 ⁺¹⁸⁵ ₋₁₇₉	4.48 ^{+0.27} _{-0.20}	-0.34 ^{+0.10} _{-0.10}	0.02 ^{+0.09} _{-0.10}	1.57	
Horo 20	43.6278	-54.0217	18.28	98.5 \pm 0.2	4954 ⁺¹⁶⁴ ₋₁₅₉	4.63 ^{+0.11} _{-0.10}	-0.60 ^{+0.05} _{-0.06}	0.08 ^{+0.04} _{-0.05}	3.00	
Horo 21	43.6917	-53.9571	19.36	67.4 \pm 1.1	5342 ⁺¹⁸⁶ ₋₁₈₀	4.95 ^{+0.12} _{-0.17}	-0.12 ^{+0.20} _{-0.14}	-0.12 ^{+0.12} _{-0.11}	2.96	
Horo 22	43.9334	-53.9473	19.02	70.0 \pm 0.6	4979 ⁺¹⁶⁷ ₋₁₆₁	4.63 ^{+0.23} _{-0.28}	-0.49 ^{+0.13} _{-0.12}	0.06 ^{+0.12} _{-0.10}	1.99	
Horo 23	43.8368	-53.9240	18.69	44.2 \pm 0.3	4821 ⁺¹⁵⁵ ₋₁₅₀	4.76 ^{+0.12} _{-0.13}	-0.43 ^{+0.07} _{-0.07}	0.25 ^{+0.06} _{-0.07}	1.73	

step is combining all the available information in order to obtain the most reliable inference on the average velocity, metallicity and their dispersions, while properly accounting for any potential foreground contamination. Figure 5 shows the radial velocity of stars versus the distance to the center of two satellites. It clearly illustrates that although the velocity signal due to the satellites is quite prominent, the contamination – albeit minor – still has to be taken into account. Thus, in order to describe the velocity distribution of each satellite we adopt the following set of mixture models (see e.g. Walker et al. 2009; Koposov et al. 2011, for similar approach).

$$P(V, \psi | \phi) = f P_{sat}(\psi) \mathcal{N}(V | V_0, \sigma) + (1 - f) P_{bg}(\psi) \mathcal{N}(V | V_{bg}, \sigma_{bg}) \quad (5)$$

Where V is the heliocentric velocity, \mathcal{N} is a Gaussian distribution, f is the fraction of objects belonging to the satellite, ϕ is the shorthand notation for the parameters of the model and ψ are ancillary variables that help us identify members (such as metallicity and/or distance from the center of the object). The key assumption is that the RV distribution for each of the satellites is Gaussian and RVs of background/foreground stars are also Gaussian distributed (a reasonable assumption given very small number of such stars).

Since each RV measurement comes with an error bar, the actual likelihood of each RV point V_i and error σ_i is the convolution of the model from Eq. 5 with the Gaussian error: $P(D|\phi) \propto \int P(V|\phi) \mathcal{N}(V|V_i, \sigma_i) dv$. Given that the underlying velocity models $P(V|\phi)$ are Gaussians themselves, the integral is trivial to analytically compute.

The ancillary parameters ψ serve the purpose of helping to separate the satellite members from the background stars. For Reticulum 2 we use $\psi = [\text{Fe}/\text{H}]$ and model the joint distribution of metallicity and RV. We assume that the metallicities of both the background and the object are Gaussian-distributed (with different means and variances): $P_{sat}([\text{Fe}/\text{H}]) = \mathcal{N}([\text{Fe}/\text{H}] | [\text{Fe}/\text{H}]_{sat}, \sigma_{[\text{Fe}/\text{H}],sat})$, $P_{bg}([\text{Fe}/\text{H}]) = \mathcal{N}([\text{Fe}/\text{H}] | [\text{Fe}/\text{H}]_{bg}, \sigma_{[\text{Fe}/\text{H}],bg})$. For Horologium 1 we have fewer potential members, so we require more information than RV and metallicity. Therefore we model the joint distribution of RV, metallicity, and distance from the center of the satellite: $\psi = \{r, [\text{Fe}/\text{H}]\}$. The metallicities are modelled as Gaussian distributions, while an exponential density model with the morphological parameters from K15 is used to represent the distance distribution of satellite member stars:

$$P_{sat}(r) = \frac{r}{h^2} \exp\left(-\frac{r}{h}\right) \quad (6)$$

where h is the exponential scale length.

The model for the background sources assumes a uniform distribution within the field $P_{bg}(r) = 2r/r_f^2$, where the r_f is the field radius.

The full list of parameters in our membership modelling for both Reticulum 2 and Horologium 1 was $f, V_{sat}, \sigma_{sat}, [\text{Fe}/\text{H}]_{sat}, \sigma_{[\text{Fe}/\text{H}],sat}$ and $V_{bg}, \sigma_{bg}, [\text{Fe}/\text{H}]_{bg}, \sigma_{[\text{Fe}/\text{H}],bg}$, respectively.

We adopt uninformative priors on $V_{sat}, V_{bg}, [\text{Fe}/\text{H}]_{sat}$

and $[\text{Fe}/\text{H}]_{bg}$, Jeffreys priors on the distribution dispersions and f . The posterior was then sampled using the ensemble MCMC sampler implemented in `Python` by Foreman-Mackey et al. (2013). The posteriors for the parameters of the satellites are shown on Figures 6 and 7. The resulting parameter measurements quoted in Table 1 are the 1D MAP values, and the uncertainties are the 68% percentiles.

4. DISCUSSION AND CONCLUSIONS

4.1. Reticulum 2

On the basis of inferred kinematics and chemistry, our analysis has unambiguously identified 18 members in Reticulum 2. Of these stars, 17 are red giants and one is a horizontal branch star.

We find an intrinsic velocity dispersion of $3.22^{+1.64}_{-0.49} \text{ km s}^{-1}$ in Reticulum 2. Although our value is slightly lower than the parallel analyses by Walker et al. (2015b) and Simon et al. (2015)³, the velocity dispersion measurements from all studies are consistent within the uncertainties. As already pointed out by Simon et al. (2015) and Walker et al. (2015b), the velocity dispersion unambiguously indicate that Reticulum 2 is a dwarf galaxy. Using the mass estimator of Wolf et al. (2010) we can estimate the total mass inside half-light radii to be $2.54^{+4.52}_{-0.32} \times 10^5 M_\odot$ for Reticulum 2, which corresponds to a mass-to-light ratio of ~ 500 . However the total mass and the mass-to-light ratio has to be treated with caution, as Reticulum 2 is very elongated (axis ratio of 0.4) and is potentially being tidally disrupted (see K15), therefore the mass estimator could be significantly biased.

We also find a substantial spread in overall metallicity of $\sigma([\text{Fe}/\text{H}]) = 0.29^{+0.13}_{-0.05} \text{ dex}$. In contrast to Simon et al. (2015), we have also inferred $[\alpha/\text{Fe}]$ abundance ratios for all satellite candidates observed through the Gaia-ESO Survey. Although the uncertainties on $[\alpha/\text{Fe}]$ are large for most of our confirmed members, we found the Reticulum 2 data tended towards high $[\alpha/\text{Fe}]$ ratios. Indeed, the lowest $[\alpha/\text{Fe}]$ ratio of our 18 confirmed members exceeds $+0.2 \text{ dex}$. The resulting estimate of $[\alpha/\text{Fe}]$ for Reticulum 2 is $[\alpha/\text{Fe}] = 0.40 \pm 0.04$, consistent with observations of well-studied present-day dwarf galaxies (Tolstoy et al. 2009; Kirby et al. 2011).

There are slight discrepancies in the estimated mean metallicity of Reticulum 2 between this study and Simon et al. (2015). Walker et al. (2015b) finds $[\text{Fe}/\text{H}] = -2.67^{+0.34}_{-0.34}$, consistent with our measurement of $[\text{Fe}/\text{H}] = -2.46^{+0.09}_{-0.10}$. Simon et al. (2015) finds a comparable value of $[\text{Fe}/\text{H}] = -2.65 \pm 0.07$ from Ca II equivalent widths. The quoted uncertainty by Simon et al. (2015) are the lowest of all studies, but given our uncertainties, $[\text{Fe}/\text{H}] = -2.65$ is a mere 1.9σ deviation. We explored this possible discrepancy by searching the Gaia-ESO Survey for HR10 and HR21 spectra of HD 122563, a well-studied metal-poor giant star. HD 122563 is a Gaia benchmark star (Jofré et al. 2014), and has atmospheric parameters comparable to the stars in Reticulum 2. The lowest S/N in any single exposure of HD 122563 was ~ 20 .

³ Simon et al. (2015) use the Gaia-ESO data as well in their analysis of Reticulum 2

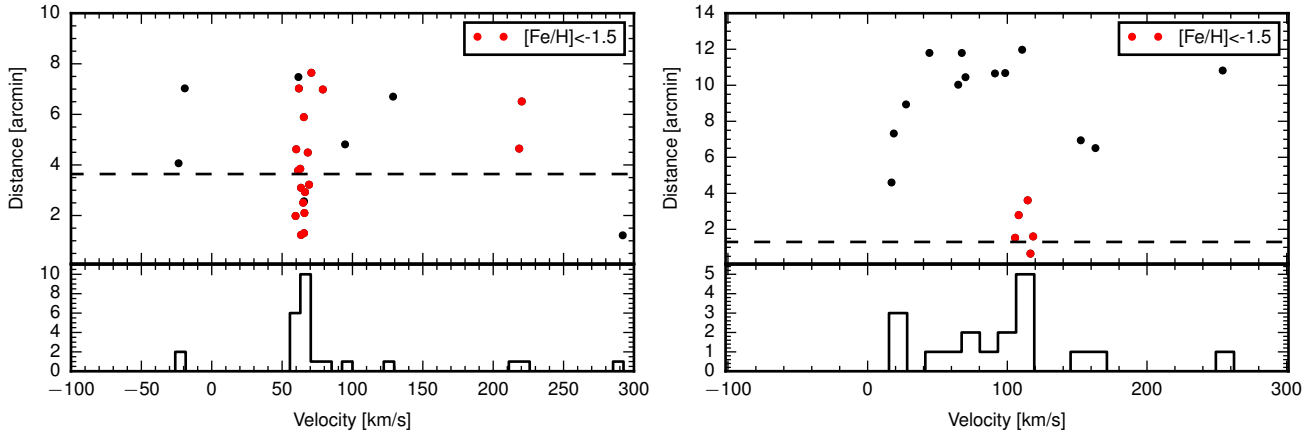


FIG. 5.— The measured RV and spatial distance from the satellite centroid for Reticulum 2 (left) and Horologium 1 (right). The bottom panels show the RV distributions. The dashed line on top panels indicates the half-light radius as measured by K15. Red circles are the stars with $[\text{Fe}/\text{H}] < -1.5$. In the case of Reticulum 2 the peak in the radial velocities at $V \sim 65 \text{ km s}^{-1}$ due to the satellite stars is obvious. In the case of Horologium 1 the peak at $V \sim 100 \text{ km s}^{-1}$ is less prominent but still significant, because all the stars in that peak are within \sim twice the half-light radius and have low metallicity as opposed to high metallicity background stars located at larger distances from the satellite center.

We analysed these data with the model described in Section 3.2, except we found it necessary to use a fourth order polynomial to account for the continuum in the HD 122563 spectra. We find a MAP $[\text{Fe}/\text{H}] = -2.79$, in good agreement with the accepted literature value of $[\text{Fe}/\text{H}] = -2.64$ (Jofré et al. 2014). If anything our metallicity scale may be ~ 0.1 dex more metal-poor than the benchmark, the opposite direction to the discrepancy in Simon et al. (2015). Nevertheless, our robust uncertainties make our measurement reasonably consistent with Walker et al. (2015b) and Simon et al. (2015).

An unexpected discovery was also made in the Gaia-ESO Survey Reticulum 2 data. The left panels of Figure 4 show the inferred radial velocity and metallicity from the model described in Section 3.2. Two stars (Reti 0 and Reti 13) are present at $V_{\text{hel}} \sim 219 \text{ km s}^{-1}$ with indistinguishable metallicities of $[\text{Fe}/\text{H}] \sim -2$. The $\log g$ is largely uninformative for these stars: the MAP values are consistent with a sub-giant star, but the uncertainties are sufficiently large that both a dwarf or sub-giant are equally plausible. We checked the Walker et al. (2015b) and Simon et al. (2015) studies for other stars at comparable velocities. We found one match in Walker et al. (2015b) (star Ret2-153 in their nomenclature), which turned out to be Reti 0, and unsurprisingly both stars were in the Simon et al. (2015) study, simply marked as ‘non-members’ of Reticulum 2. A subsequent search in the surrounding Gaia-ESO Survey Milky Way field (e.g., non-Reticulum 2 candidates that were in the same field) revealed a further two stars $(\alpha, \delta) = (53.69300, -54.17860)$ and $(53.73709, -54.10720)$ with similar systemic velocities to Reti 0 and Reti 13 (223.7 km s^{-1} , 221.3 km s^{-1}). We have not inferred stellar parameters for these additional two stars. However, if we ignore the information that Reti 0 and Reti 13 have indistinguishable metallicities, a simple calculation using the average number of stars per km s^{-1} at $\text{RV} \sim 200 \text{ km s}^{-1}$ gives the significance of having 4 stars within $\sim 5 \text{ km s}^{-1}$ to be $\sim 99.5\%$ (after correcting for “look-elsewhere” effect, e.g. Gross & Vitells 2010). Analogous to the 300 km s^{-1} stream near Segue 1 (Geha et al. 2009; Norris et al. 2010; Frebel et al.

2013), this kinematic feature is yet another reminder of the highly substructured nature of the Milky Way halo (e.g., Schlaufman et al. 2009; Starkenburg et al. 2009).

4.2. Horologium 1

With only 5 confirmed members in Horologium 1, we are far more sensitive to stochastic sampling effects than what we are for Reticulum 2. Nevertheless, we find a large kinematic dispersion of $4.9^{+2.8}_{-0.9} \text{ km s}^{-1}$ and a metallicity dispersion of $0.17^{+0.2}_{-0.03}$, firmly grouping Horologium 1 with other known dwarf galaxies. Note that our posteriors on $\sigma(V)$ and $\sigma([\text{Fe}/\text{H}])$ have considerable asymmetry towards higher velocity and metallicity dispersions, which is primarily attributable to the low number of confirmed members in our sample. When more data becomes available, it is reasonable to expect that a larger metallicity dispersion may be found for Horologium 1, as our MAP $\sigma([\text{Fe}/\text{H}])$ is the lowest reported measurement for comparable ultra-faint dwarf galaxies (Figure 8). A lower metallicity dispersion is strongly disfavoured by our data, and would be inconsistent with the large velocity dispersion we observe. We also find Horologium 1 to have $[\alpha/\text{Fe}] = 0.30 \pm 0.07$, consistent with the Milky Way dwarf galaxy population.

According to the mass estimator of Wolf et al. (2010) we estimate the total mass inside the half-light radii of Horologium 1 is $5.25^{+11.5}_{-0.78} \times 10^5 M_{\odot}$ (notice however a very big error bar). The mass-to-light ratio of ~ 600 is similar to that observed in Reticulum 2.

4.3. Comparison to other ultra-faints

Overall both Reticulum 2 and Horologium 1 systems seem to be quite representative samples of the other known ultra-faint dwarf galaxies.

- The average metallicity of stars in both systems is very low (one of the lowest among dwarf galaxies), but both dwarfs lie well on the existing mass/luminosity - metallicity correlation (see bottom left panel of Figure 8).
- The metallicity spread, although uncertain, is significantly different from zero, matching what is ob-

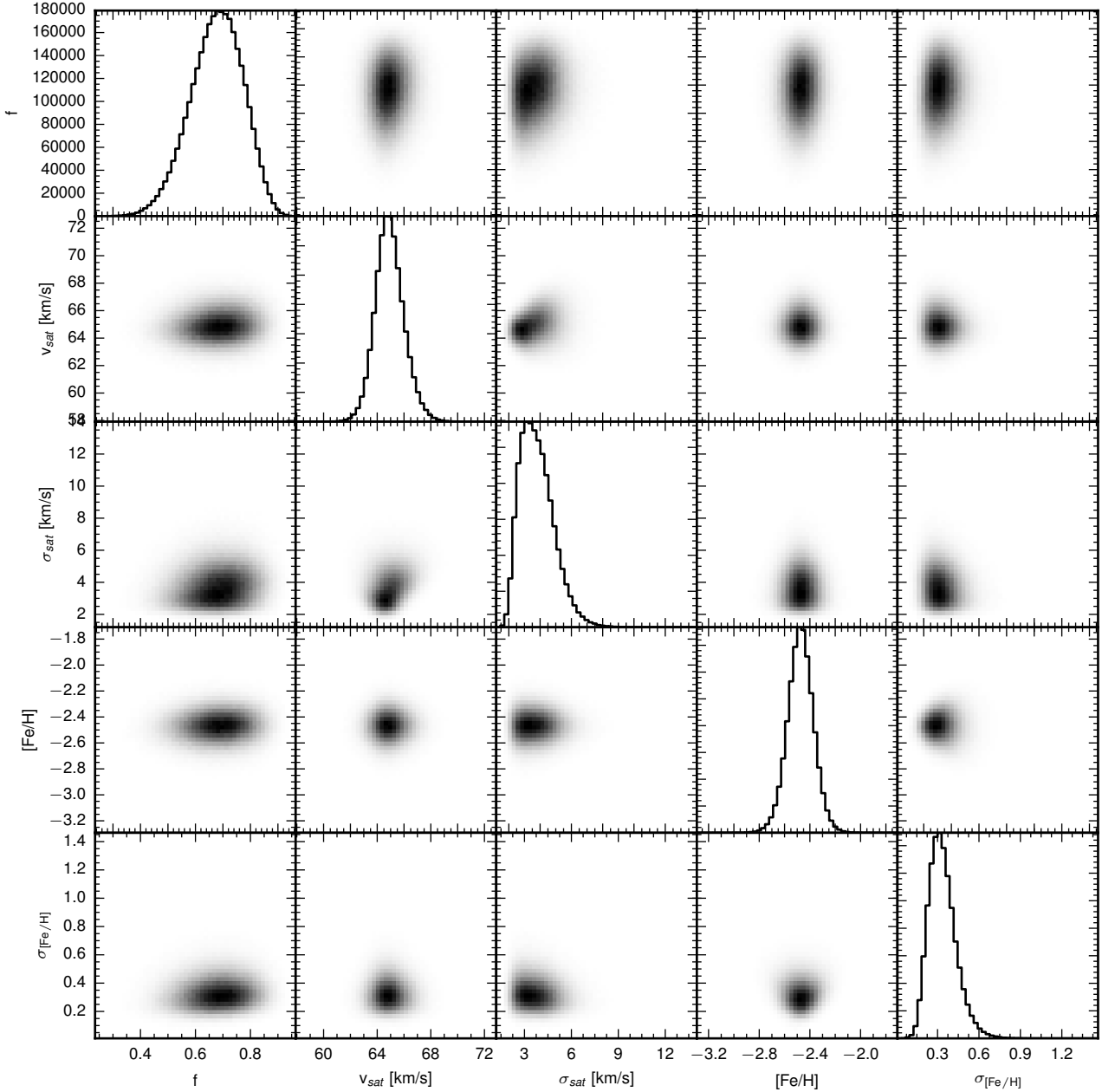


FIG. 6.— 2D and 1D marginalized posteriors for the parameters of the chemo-dynamical modeling of Reticulum 2

served in other dwarf galaxies (top left panel of Figure 8). It is possible though that the spread seen in Horologium 1 and Reticulum 2 is somewhat smaller than the spread of 0.5–0.7 dex observed in other ultra-faint systems such as Segue 1 (Simon et al. 2011), but this could simply be a result of small sample sizes.

- The dark matter content and the mass-to light ratio in the observed systems seem to agree well with the existing correlations with galaxy luminosity (right panel of Figure 8). This suggests that even with these new discoveries of ultra-faint dwarfs we have not reached the limiting density scale of dark matter, which would inform us about the elusive properties of dark matter (Gilmore et al. 2007).

4.4. Possible association with the Magellanic Clouds

Given their proximity to the LMC and the SMC on the sky, there exists an exhilarating possibility that some of the newly discovered satellites, including Reticulum 2 and Horologium 1, have once been part of the Great Magellanic Family. If such a connection proves true, there is hope to link the internal properties of the dwarfs (e.g., their dark matter content, the star-formation and the enrichment histories) with their orbital motion before and during the accretion onto the Milky Way. Thus, finally, an in-depth self-consistent picture of the UFS formation and evolution can be assembled.

Considering the total number of satellites discovered in the SDSS, VST ATLAS and PanSTARRs surveys, the relatively small patch of sky covered by the first year

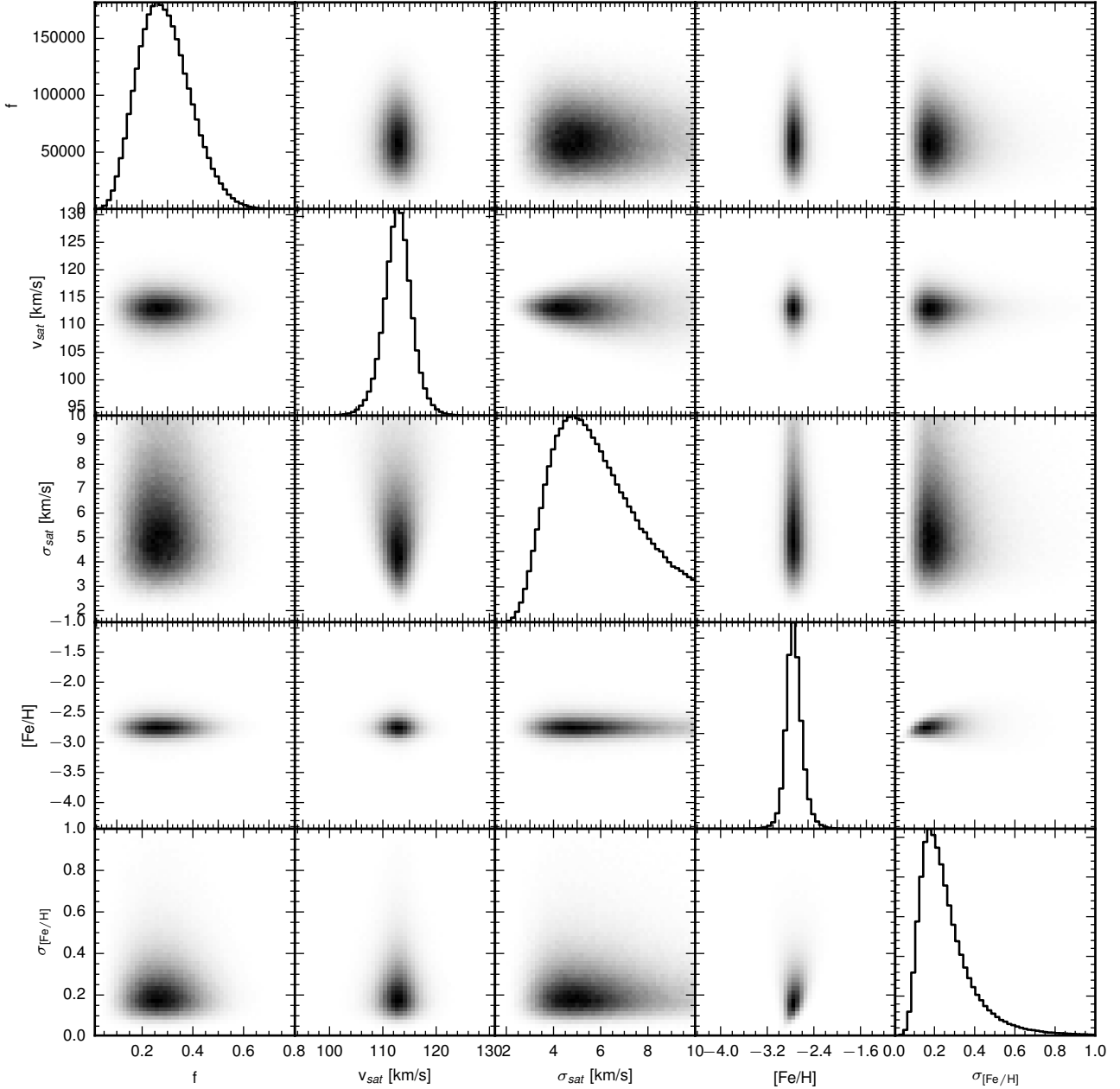


FIG. 7.— 2D and 1D marginalized posteriors for the parameters of the chemo-dynamical modeling of Horologium 1

of DES observations appears unusually rich in satellites. According to K15, the over-density of satellites around the Magellanic Clouds is moderate but significant, with at least 3-4 objects possibly belonging to the LMC/SMC pair. Note however, that the above calculation does not account for the fact that for the faintest systems (e.g., direct analogs of Reticulum 2 and Horologium 1), the SDSS census is incomplete beyond 50 kpc. Therefore the number of faintest dwarfs within the DES footprint – namely those with $M_V > -4$ – have to be estimated under the assumption of their Galacto-centric radial distribution. Given perfect freedom, it seems plausible to find a radial profile flat enough to produce as many faint satellites as have been discovered in the DES data. This, however, would seem to be in tension with the lack of discoveries from surveys like VST ATLAS and PanSTARRs. In

the absence of completeness estimates for the ongoing imaging surveys, we attempt to clarify the connection between the newly discovered satellites and the Magellanic Clouds by complementing their 3D positions with the radial velocity measurements obtained with the VLT.

The satellites' kinematics can be compared to predictions made from cosmological zoom-in simulations. For example, according to Sales et al. (2011), the distribution of the satellites in phase-space reveals the time of accretion of the Magellanic system. By finding one suitable LMC analog in the high-resolution Aquarius suite (Springel et al. 2008), Sales et al. (2011) convincingly demonstrate that a high concentration of the former LMC companions is expected in the Cloud's vicinity if the LMC has only had one peri-center crossing. More recently, a systematic analysis of 25 LMC analogs in

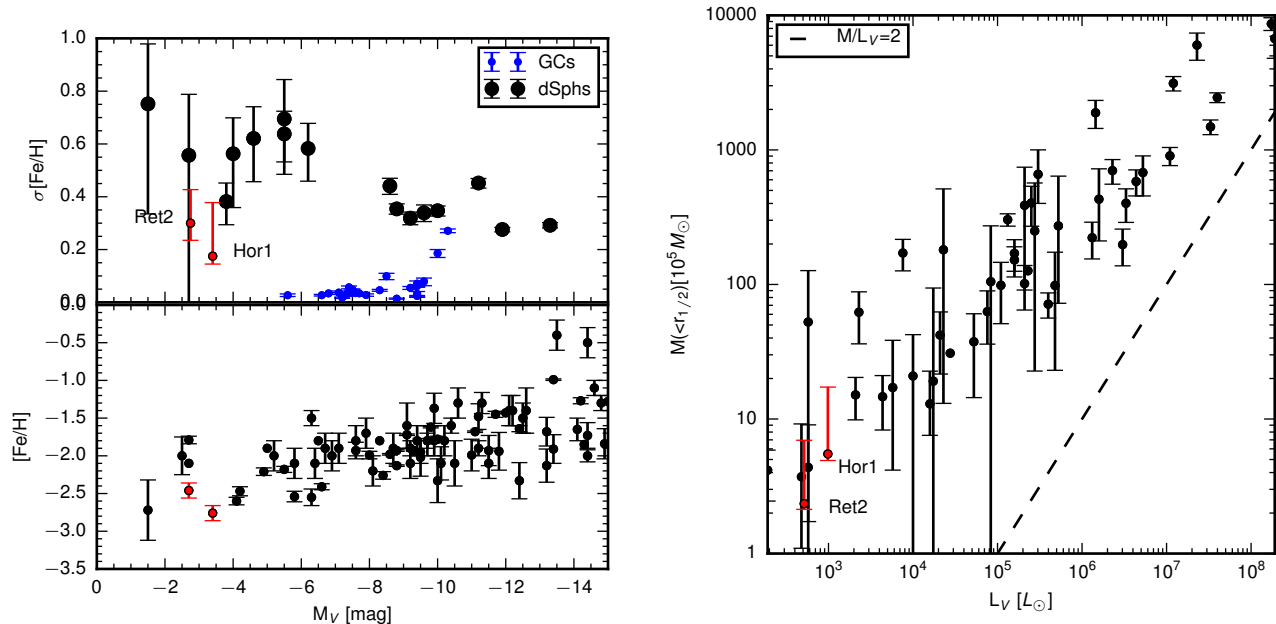


FIG. 8.— *Left panel.* Mean metallicity (bottom panel) and metallicity spread (top panel) as a function of luminosity for faint stellar systems. The data from McConnachie (2012); Willman & Strader (2012) were used. The measurements of Horologium 1 and Reticulum 2 are shown by red circles. Our measurements confirm that these recently discovered galaxies extend the existing mass metallicity trends, and show significant spreads in abundances similar to the ones observed among other dwarf galaxies and not in globular clusters. *Right panel.* The dynamical mass inside half-light radius vs galaxy luminosity. Both Reticulum 2 and Horologium 1 are on the very faint end of the existing relationship. The dashed line shows the dynamical mass expected for the stellar population with $M/L_V=2$ (i.e., without dark matter).

the ELVIS suite of cosmological zoom-in simulations has been presented by Deason et al. (2015). Here, rather than a report on a case study, an evidence for a trend between the $z=0$ phase-space scatter of the LMC satellites' and the group in-fall time is presented. According to Deason et al. (2015), the observed distribution of satellites discovered in the DES data appears consistent with a recent, i.e. <2 Gyr, accretion. For such late events, the authors also provide a rough estimate of the total number of past LMC satellites in the DES footprint: based on positions alone, there should be at least 4 such objects in the current DES sample. Both Sales et al. (2011) and Deason et al. (2015) emphasize the role that kinematics play in uncovering the origin of the Milky Way satellites: chance spatial alignments are possible, however these are in general less likely in the vicinity of the group's central (e.g., in the LMC).

The benefit of these N-body simulations is that they paint a fully consistent cosmological portrait of the Magellanic Group, both in terms of accretion history as well as the amount of expected substructure. However, it is obvious that these simulations cannot match either the exact orbit of the LMC nor the presence of its massive companion, the SMC. To complement the cosmological N-body zoom-in runs, controlled simulations of LMC/SMC accretion can be mass-produced for a much larger range of the in-fall parameters (e.g., Nichols et al. 2011). We will describe the outcome of such an experiment in the future (see Jethwa et al., in prep.). Meanwhile, we can shed some light onto possible links between the Magellanic Clouds and Reticulum 2 or Horologium 1 by comparisons with the observed kinematics of the Magellanic gaseous Stream (MS). The stream of neutral hydrogen emanating from the Clouds has been mapped out

across tens of degrees, and is complemented with well-documented kinematics (see e.g., Putman et al. 2003; Nidever et al. 2008). Additionally, several numerical models exist explaining the genesis of the MS (see e.g., Besla et al. 2010; Diaz & Bekki 2012).

Figure 9 shows the positions of the two satellites in the space of MS longitude L_{MS} , MS latitude B_{MS} and radial velocity. The top left panel of the figure gives the locations of Reticulum 2 and Horologium 1 with respect to the distribution of the column density of H I gas in the Magellanic stream as detected by Nidever et al. (2008). We split the H I detections into three bins according to the latitude B_{MS} , marked with red ($0^\circ < B_{\text{MS}} < 14^\circ$), green ($-9^\circ < B_{\text{MS}} < 0^\circ$) and blue ($-23^\circ < B_{\text{MS}} < -9^\circ$) colors. The location of Reticulum 2 (Horologium 1) is also shown as blue (red) filled circle. The top right panel presents the false-RGB composite map of H I in the plane of the MS longitude L_{MS} and heliocentric radial velocity V_{LSR} . As previously shown by Nidever et al. (2008), in this projection the Stream's H I content forms a broad band, typically $\sim 100 \text{ km s}^{-1}$ in extent. As indicated by the rapidly changing color, portions of the stream at varying B_{MS} contribute different amounts of velocity signal at given L_{MS} . Note however that the steep velocity gradient as a function of the MS longitude is predominantly caused by the Solar reflex motion. This is confirmed in the bottom left panel of Figure 9 which displays the map of H I in the plane of L_{MS} and Galacto-centric radial velocity V_{GSR} . The V_{GSR} signature of the stream remains largely constant up to $L_{\text{MS}} \sim -40^\circ$ where it starts to decline, but slower than with respect to V_{LSR} .

As obvious from both velocity maps described above, the MS H I is detected near the positions of Reticulum 2 and Horologium 1 in the (L_{MS}, V) plane. However, the

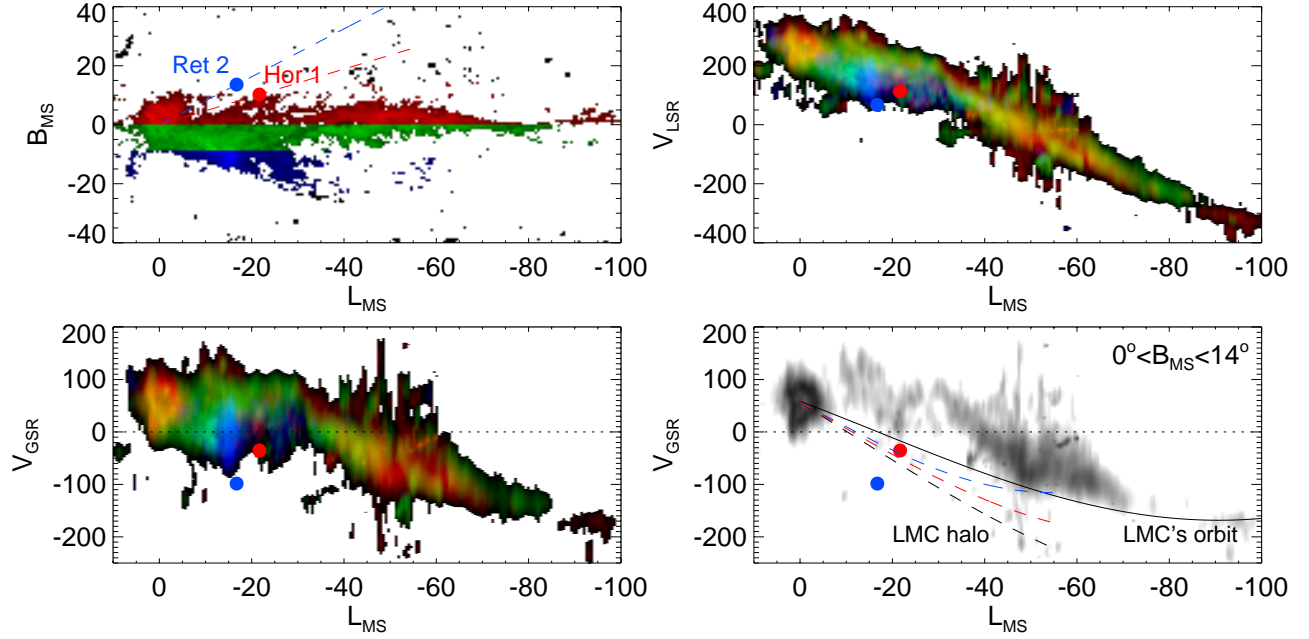


FIG. 9.— Comparison of the kinematics of Reticulum 2, Horologium 1 and the Magellanic Stream. *Top Left*: Column density of H I in the MS as detected by Nidever et al. (2008) projected in the MS coordinate system (L_{MS} , B_{MS}). For further exploration, the gas is split into three bins in latitude B_{MS} , shown in red ($0^\circ < B_{\text{MS}} < 14^\circ$), green ($-9^\circ < B_{\text{MS}} < 0^\circ$) and blue ($-23^\circ < B_{\text{MS}} < -9^\circ$) color. The location of Reticulum 2 (Horologium 1) are shown by the blue (red) filled circle. Blue (red) dashed line marks the locations of the LMC halo chosen for the line-of-sight velocity predictions that are displayed in the bottom right panel. *Top Right*: Heliocentric radial velocity V_{LSR} as a function of the MS longitude L_{MS} . The MS H I gas density in this phase-space projection is shown as a false-color RGB composite built with grey-scale density distributions from corresponding B_{MS} bins shown in the left panel. Note the strong V_{LSR} velocity gradient, which is chiefly caused by the Solar reflex motion. Both Reticulum 2 and Horologium 1 appear to lie close to the lower envelope of the MS velocity signal. *Bottom Left*: Same as the top right panel, but for Galactocentric radial velocity V_{GSR} as a function of the MS longitude L_{MS} . Note that the transformation from the LSR to the GSR has significantly reduced the velocity gradient observed in the top right panel. While the velocities of Reticulum 2 and Horologium 1 are consistent with the lower range of the MS stream kinematics at the corresponding L_{MS} , the gas with comparable V_{GSR} is located mostly at $B_{\text{MS}} < 0^\circ$, evidenced by the blue color of the region of the MS nearest to the satellites. This is further illustrated in the bottom right panel. *Bottom Right*: Motions of the MS gas with $0^\circ < B_{\text{MS}} < 14^\circ$. This map confirms that near Reticulum 2, the MS H I gas motions are different by approximately 100 km s^{-1} . On the hand, near Horologium 1, there exists MS H I gas whose velocity is similar to that of the dwarf. The black solid line is the track of the LMC's orbit (see K15). Dashed curves show the prediction for mean velocity of the LMC halo, i.e. the projection of the LMC's velocity vector onto the line-of-sight. Black dashed curve corresponds to the lines of sight crossing the LMC halo at $L_{\text{MS}} = 0^\circ$, and the blue and red dashed curves correspond to the halo slices shown in the top and left panels. Reticulum 2 is $\sim 80 \text{ km s}^{-1}$ away from the halo prediction. However, Horologium 1 is a mere $\sim 15 \text{ km s}^{-1}$ away from the halo prediction.

region of phase-space occupied by the dwarfs is dominated by the gas at negative B_{MS} (i.e., around the SMC) as evidenced by the blue tint of this portion of the image. The bottom right panel of Figure 9 illustrates the range of possible velocities of the MS with positive B only (i.e., those around Reticulum 2 and Horologium 1). At the longitude of Reticulum 2, there is a gap of order of 100 km s^{-1} between the grey-scale density map of the MS H I and the velocity of Reticulum 2. However near Horologium 1, the MS gas completely extends to the measured velocity of the satellite.

The offset in the line-of-sight velocity between the trailing MS H I and the satellites is expected, as stripped gas can experience a drag force through interactions with the hot Galactic corona. The drag will decelerate the stream clouds, causing them to fall to lower Galactocentric radii. To make sense of the radial velocities of Reticulum 2 and Horologium 1, let us recall their locations with respect to the Milky Way center and the Magellanic Clouds. In 3D space, Reticulum 2 is in front of the Clouds, $\sim 24 \text{ kpc}$ away from the LMC and $\sim 39 \text{ kpc}$ from the SMC, while Horologium 1 is behind the Clouds, $\sim 38 \text{ kpc}$ away from the LMC and $\sim 32 \text{ kpc}$ from the SMC. Importantly, both satellites are trailing the LMC, as evidenced from the

Cloud's orbital motion shown in Figure 20 of K15.

The black solid line in the bottom right panel of Figure 9 shows the projection of a backward-integrated LMC orbit from K15, namely the one with the NFW's concentration $c = 10$, projected onto the plane of L_{MS} and V_{GSR} . The orbit attains negative line-of-sight velocities at $L_{\text{MS}} < -20^\circ$ and appears to be in reasonable agreement with the velocity of Horologium 1 at the corresponding MS longitude. This implies that the 4D coordinate of Horologium 1 is consistent with those expected for the LMC's trailing debris. At the location of Reticulum 2 the velocity gap of $\sim 100 \text{ km s}^{-1}$ persists. It is tempting to assert that this precludes the possibility of an association between Reticulum 2 and the LMC. However, it is unrealistic to expect Reticulum 2 to behave simply like the LMC trailing debris. During tidal disruption it is normal to expect the trailing debris to form from particles with higher energy and angular momentum than the progenitor. Subsequently the trailing debris also have larger Galactocentric radii on average, and longer orbital periods. Yet, we know that Reticulum 2 is closer to the Milky Way's center than the LMC itself. Thus, in order to explain its origin as part of the Magellanic family, an additional factor needs to be included.

It is conceivable that an interaction with the SMC would be sufficient to drive Reticulum 2 onto its current orbit.

Finally, we have not yet considered the possibility that Reticulum 2 and/or Horologium 1 could still be bound to the LMC. Superficially, such situation seems unlikely given the distances between the LMC and the two satellites. However, Muñoz et al. (2006) report spectroscopically confirmed detection of the likely LMC's stellar halo some 22° degrees away from the LMC, at angular distances comparable to Reticulum 2 and Horologium 1. Motivated by this discovery, we test whether the line-of-sight velocities of Reticulum 2 and Horologium 1 are consistent with the LMC's halo. The dashed lines in the bottom right panel of Figure 9 show projections of the LMC velocity vector onto several lines-of-sight. The black dashed curve corresponds to the lines-of-sight slicing the LMC's halo at $L_{\text{MS}} = 0^\circ$. Blue (red) dashed curve shows the run of the projection of the mean LMC's halo velocity along the line-of-sight moving from the LMC's center to the location of Reticulum 2 (Horologium 1) as shown in the top left panel of the figure. At the position of Reticulum 2, the line-of-sight velocity of non-rotating LMC's halo would be $\sim -20 \text{ km s}^{-1}$, some $\sim 80 \text{ km s}^{-1}$ away the Galactocentric velocity of Reticulum 2, $V_{\text{GSR}}^{\text{Ret}2} \sim -100 \text{ km s}^{-1}$. However, at the position of Horologium 1, the LMC's halo's line-of-sight velocity is predicted to be $\sim -50 \text{ km s}^{-1}$, only 15 km s^{-1} away from the Galactocentric velocity of the satellite $V_{\text{GSR}}^{\text{Hor}1} \sim -35 \text{ km s}^{-1}$. It is important to note that while Horologium 1 is located at a similar angular distance from the LMC as compared to the stellar halo detections reported by Muñoz et al. (2006), it is probably twice as far away from the LMC in 3D, i.e. 40 kpc instead of 20 kpc. To explain the dynamics of the LMC+SMC system and the formation of the MS, Besla et al. (2010) advocate the existence of a massive ($M_{\text{vir}} = 3 \times 10^{11} M_\odot$) dark matter halo of the LMC. The corresponding virial

radius of this halo would be $> 100 \text{ kpc}$, while its (approximate) tidal radius just under 40 kpc. If the LMC is on its first pericenter crossing, then given the weak tides the LMC has been experiencing so far, it is reasonable to expect that its dark matter distribution can extend as far as 40 kpc. Therefore, surprisingly, there appears to be some probability that Horologium 1 is still gravitationally bound to the Large Magellanic Cloud.

Based on data products from observations made with ESO Telescopes at the La Silla Paranal Observatory under programme ID 188.B-3002. These data products have been processed by the Cambridge Astronomy Survey Unit (CASU) at the Institute of Astronomy, University of Cambridge, and by the FLAMES/UVES reduction team at INAF/Osservatorio Astrofisico di Arcetri. These data have been obtained from the Gaia-ESO Survey Data Archive, prepared and hosted by the Wide Field Astronomy Unit, Institute for Astronomy, University of Edinburgh, which is funded by the UK Science and Technology Facilities Council.

This work was partly supported by the European Union FP7 programme through ERC grant numbers 320360 and 308024 and by the Leverhulme Trust through grant RPG-2012-541. We acknowledge the support from INAF and Ministero dell'Istruzione, dell'Università e della Ricerca (MIUR) in the form of the grant "Premiale VLT 2012". The results presented here benefit from discussions held during the Gaia-ESO workshops and conferences supported by the ESF (European Science Foundation) through the GREAT Research Network Programme.

We thank Matt Walker, Mario Mateo, Gurtina Besla, David Nidever, Bertrand Plez, Matthew Ruffoni and Juliet Pickering.

This research made use of Astropy, a community-developed core Python package for Astronomy (Astropy Collaboration et al. 2013).

REFERENCES

- Abazajian, K. N., Adelman-McCarthy, J. K., Agüeros, M. A., et al. 2009, *ApJS*, 182, 543
- Alam, S., Albareti, F. D., Allende Prieto, C., et al. 2015, *arXiv:1501.00963*
- Alvarez, R., & Plez, B. 1998, *A&A*, 330, 1109
- Astropy Collaboration, Robitaille, T. P., Tollerud, E. J., et al. 2013, *A&A*, 558, AA33
- Balbinot, E., Santiago, B. X., da Costa, L., et al. 2013, *ApJ*, 767, 101
- Belokurov, V., Zucker, D. B., Evans, N. W., et al. 2006, *ApJ*, 647, L111
- Belokurov, V., Zucker, D. B., Evans, N. W., et al. 2007, *ApJ*, 654, 897
- Belokurov, V., Evans, N. W., Irwin, M. J., et al. 2007, *ApJ*, 658, 337
- Belokurov, V., Walker, M. G., Evans, N. W., et al. 2008, *ApJ*, 686, L83
- Belokurov, V., Walker, M. G., Evans, N. W., et al. 2009, *MNRAS*, 397, 1748
- Belokurov, V., Walker, M. G., Evans, N. W., et al. 2010, *ApJ*, 712, L103
- Belokurov, V. 2013, *New A Rev.*, 57, 100
- Belokurov, V., Irwin, M. J., Koposov, S. E., et al. 2014, *MNRAS*, 441, 2124
- Plez, B. 2012, *Astrophysics Source Code Library*, 1205.004
- Besla, G., Kallivayalil, N., Hernquist, L., et al. 2010, *ApJ*, 721, L97
- Bressan, A., Marigo, P., Girardi, L., et al. 2012, *MNRAS*, 427, 127
- Casey, A. R., Keller, S. C., & Da Costa, G. 2012, *AJ*, 143, 88
- Casey, A. R., Da Costa, G., Keller, S. C., & Maunder, E. 2013, *ApJ*, 764, 39
- Casey, A. R., Keller, S. C., Da Costa, G., Frebel, A., & Maunder, E. 2014, *ApJ*, 784, 19
- Deason, A. J., Belokurov, V., Hamren, K. M., et al. 2014, *MNRAS*, 444, 3975
- Deason, A. J., Wetzel, A. R., Garrison-Kimmel, S., & Belokurov, V. 2015, *arXiv:1504.04372*
- de Boer, T. J. L., Belokurov, V., Beers, T. C., & Lee, Y. S. 2014, *MNRAS*, 443, 658
- Diaz, J. D., & Bekki, K. 2012, *ApJ*, 750, 36
- D'Onghia, E., & Lake, G. 2008, *ApJ*, 686, L61
- de Laverny, P., Recio-Blanco, A., Worley, C. C., & Plez, B. 2012, *A&A*, 544, AA126
- Foreman-Mackey, D., Hogg, D. W., Lang, D., & Goodman, J. 2013, *PASP*, 125, 306
- Frebel, A., Lunnan, R., Casey, A. R., et al. 2013, *ApJ*, 771, 39
- Geha, M., Willman, B., Simon, J. D., et al. 2009, *ApJ*, 692, 1464
- Geringer-Sameth, A., Walker, M. G., Koushiappas, S. M., et al. 2015, *arXiv:1503.02320*
- Gilmore, G., Wilkinson, M. I., Wyse, R. F. G., et al. 2007, *ApJ*, 663, 948
- Gilmore, G., Randich, S., Asplund, M., et al. 2012, *The Messenger*, 147, 25

- Goodman, J., & Weare, J. 2010, *Comm. Appl. Math. Comp. Sci.*, 5, 65
- Grillmair, C. J. 2009, *ApJ*, 693, 1118
- Grillmair, C. J. 2014, *ApJ*, 790, L10
- Gross, E., & Vitells, O. 2010, *European Physical Journal C*, 70, 525
- Gustafsson, B., Edvardsson, B., Eriksson, K., et al. 2008, *A&A*, 486, 951
- Heiter, et al. 2015, in preparation.
- Husser, T.-O., Wende-von Berg, S., Dreizler, S., et al. 2013, *A&A*, 553, A6
- Irwin, M. J., Belokurov, V., Evans, N. W., et al. 2007, *ApJ*, 656, L13
- Jofré, P., Heiter, U., Soubiran, C., et al. 2014, *A&A*, 564, A133
- Kim, D., & Jerjen, H. 2015, *ApJ*, 799, 73
- Kim, D., Jerjen, H., Milone, A. P., Mackey, D., & Da Costa, G. S. 2015, *ApJ*, 803, 63
- Kim, D., Jerjen, H., Mackey, D., Da Costa, G. S., & Milone, A. P. 2015, arXiv:1503.08268
- Kirby, E. N., Guhathakurta, P., & Sneden, C. 2008, *ApJ*, 682, 1217
- Kirby, E. N., Lanfranchi, G. A., Simon, J. D., Cohen, J. G., & Guhathakurta, P. 2011, *ApJ*, 727, 78
- Kirby, E. N., Boylan-Kolchin, M., Cohen, J. G., et al. 2013, *ApJ*, 770, 16
- Koleva, M., Prugniel, P., Bouchard, A., & Wu, Y. 2009, *A&A*, 501, 1269
- Koposov, S., de Jong, J. T. A., Belokurov, V., et al. 2007, *ApJ*, 669, 337
- Koposov, S. E., Gilmore, G., Walker, M. G., et al. 2011, *ApJ*, 736, 146
- Koposov, S. E., Belokurov, V., & Wyn Evans, N. 2013, *ApJ*, 766, 79
- Koposov, S. E., Belokurov, V., Torrealba, G., & Wyn Evans, N. 2015, arXiv:1503.02079, *ApJ* accepted
- Laevens, B. P. M., Martin, N. F., Ibata, R. A., et al. 2015, *ApJ*, 802, L18
- Lee, Y. S., Beers, T. C., Sivarani, T., et al. 2008, *AJ*, 136, 2022
- Lee, D. M., Johnston, K. V., Sen, B., & Jessop, W. 2015, *ApJ*, 802, 48
- Lewis, et al. 2015, in preparation.
- Martin, N. F., Ibata, R. A., Chapman, S. C., Irwin, M., & Lewis, G. F. 2007, *MNRAS*, 380, 281
- Martin, C., Carlin, J. L., Newberg, H. J., & Grillmair, C. 2013, *ApJ*, 765, L39
- Martin, N. F., Nidever, D. L., Besla, G., et al. 2015, arXiv:1503.06216
- McConnachie, A. W. 2012, *AJ*, 144, 4
- Muñoz, R. R., Majewski, S. R., Zaggia, S., et al. 2006, *ApJ*, 649, 201
- Muñoz, R. R., Carlin, J. L., Frinchaboy, P. M., et al. 2006, *ApJ*, 650, L51
- Nelder, J. A., & Mead, R. 1965, *The Computer Journal*, 7, 308
- Nichols, M., Colless, J., Colless, M., & Bland-Hawthorn, J. 2011, *ApJ*, 742, 110
- Nidever, D. L., Majewski, S. R., & Burton, W. B. 2008, *ApJ*, 679, 432
- Norris, J. E., Wyse, R. F. G., Gilmore, G., et al. 2010, *ApJ*, 723, 1632
- Pasquini, L., Avila, G., Blecha, A., et al. 2002, *The Messenger*, 110, 1
- Putman, M. E., Staveley-Smith, L., Freeman, K. C., Gibson, B. K., & Barnes, D. G. 2003, *ApJ*, 586, 170
- Randich, S., Gilmore, G., & Gaia-ESO Consortium 2013, *The Messenger*, 154, 47
- Ruffoni, M. P., Den Hartog, E. A., Lawler, J. E., et al. 2014, *MNRAS*, 441, 3127
- Sales, L. V., Navarro, J. F., Cooper, A. P., et al. 2011, *MNRAS*, 418, 648
- Schlaufman, K. C., Rockosi, C. M., Allende Prieto, C., et al. 2009, *ApJ*, 703, 2177
- Simon, J. D., Geha, M., Minor, Q. E., et al. 2011, *ApJ*, 733, 46
- Simon, J. D., Drlica-Wagner, A., Li, T. S., et al. 2015, arXiv:1504.02889
- Smiljanic, R., Korn, A. J., Bergemann, M., et al. 2014, *A&A*, 570, AA122
- Springel, V., Wang, J., Vogelsberger, M., et al. 2008, *MNRAS*, 391, 1685
- Starkenbourg, E., Helmi, A., Morrison, H. L., et al. 2009, *ApJ*, 698, 567
- Tollerud, E. J., Beaton, R. L., Geha, M. C., et al. 2012, *ApJ*, 752, 45
- Tolstoy, E., Hill, V., & Tosi, M. 2009, *ARA&A*, 47, 371
- The Dark Energy Survey Collaboration 2005, arXiv:astro-ph/0510346
- The DES Collaboration, Bechtol, K., Drlica-Wagner, A., et al. 2015, arXiv:1503.02584
- The Fermi-LAT Collaboration, The DES Collaboration, :, et al. 2015, arXiv:1503.02632
- Walker, M. G., Mateo, M., Olszewski, E. W., Sen, B., & Woodroffe, M. 2009, *AJ*, 137, 3109
- Walker, M. G., Olszewski, E. W., & Mateo, M. 2015, *MNRAS*, 448, 2717
- Walker, M. G., Mateo, M., Olszewski, E. W., et al. 2015, arXiv:1504.03060
- Walsh, S. M., Jerjen, H., & Willman, B. 2007, *ApJ*, 662, L83
- Willman, B., Blanton, M. R., West, A. A., et al. 2005a, *AJ*, 129, 2692
- Willman, B., Dalcanton, J. J., Martinez-Delgado, D., et al. 2005b, *ApJ*, 626, L85
- Willman, B. 2010, *Advances in Astronomy*, 2010, 285454
- Willman, B., & Strader, J. 2012, *AJ*, 144, 76
- Wolf, J., Martinez, G. D., Bullock, J. S., et al. 2010, *MNRAS*, 406, 1220
- Zucker, D. B., Belokurov, V., Evans, N. W., et al. 2006, *ApJ*, 643, L103
- Zucker, D. B., Belokurov, V., Evans, N. W., et al. 2006, *ApJ*, 650, L41